AIChE Journal
DOI10.1002/aic.16687

Optimizing Catalyst Pore Network Structure in the Presence of Deactivation by Coking

Guanghua Ye [a], Haizhi Wang [a], Xinggui Zhou [a, *], Frerich J. Keil [b, †], Marc-Olivier Coppens [c, ‡], Weikang Yuan [a]

[a] State Key Laboratory of Chemical Engineering, East China University of Science and Technology, Shanghai 200237, China

[b] Institute of Chemical Reaction Engineering, Hamburg University of Technology, Hamburg D-21073, Germany

[c] Dept. of Chemical Engineering, University College London, London WC1E 7JE, UK

[*] Co-corresponding author. Email address: xgzhou@ecust.edu.cn

[†] Co-corresponding author. Email address: keil@tuhh.de

‡ Co-corresponding author. Email address: m.coppens@ucl.ac.uk

Received: Feb 19, 2019;Revised: May 13, 2019;Accepted: Jun 04, 2019

ABSTRACT

Designing the pore network structure is an effective approach to improve the performance of industrial catalyst particles, although it receives less attention than designing catalytic surfaces or active sites. This work presents a first example of the optimization of catalyst pore network structures in the presence of deactivation by coke formation, using a three-dimensional pore network model. Propane dehydrogenation in a Pt-Sn/Al_2O_3 catalyst particle is taken as the model reaction system. Catalyst particles with unimodal and bimodal pore size distributions are investigated, both being commonly used in industry. The porosity, connectivity, pore size, and their spatial distributions are optimized under two separate assumptions: constant intrinsic activity per unit catalyst weight and constant intrinsic activity per unit internal surface area. The optimized catalyst shows up to 14-fold improvement in the time-averaged propene formation rate, when compared to a benchmark catalyst. This significant improvement is primarily because of reductions in diffusion resistance and pore blockage.

Keywords: *propane dehydrogenation, deactivation by coking, pore network model, catalyst design, optimization*

Introduction

The design of industrial, supported heterogeneous catalysts involves the catalytically active phase (e.g., in the form of nanocrystals with various facets), as well as the catalyst support (size, shape and pore network structure)[1,2]. The former, nanoscale problem has been extensively investigated, and considerable progress has been made; the latter, mesoscale problem receives less attention, although such research is also very important in developing industrial catalysts with high activity, selectivity, and stability[1]. On the one hand, the nanoporous structure provides for a large internal surface area to well dispersed catalytic active sites (e.g., metals like Pt), yet, on the other hand, it also causes strong diffusion resistance due to confinement effects. Strong diffusion resistance leads to steep concentration gradients of products and reactants, which can significantly reduce the activity, selectivity, and stability of catalyst particles. Thus, to achieve an industrial catalyst with high performance, it is essential to properly design its pore network structure.

The benefits of designing the catalyst pore network structure has been pointed out in several works. For example, Beeckman and Hegedus[3] computationally optimized the mesopore size and mesoporosity of a deNO_x catalyst, and they found that the optimized catalyst showed up to 50% improvement in volumetric activity. Keil and Rieckmann[1,4] performed extensive numerical optimizations of a hydrodemetalation catalyst, and a significant increase in activity was observed after optimizing the mesopore size and mesoporosity. Wang and Coppens[5,6] introduced optimal macroporosity into the mesoporous catalysts for deNO_x and autothermal reforming of methane, and they found that the computationally optimized macro–mesoporous catalysts for the two

reaction systems could be 80-180% and 40-300% more active, respectively, as well as allow to tune the H_2/CO ratio in the case of autothermal reforming. More recently, Wei[7] introduced an additional material with high fluid diffusivity into a catalyst particle and numerically optimized this composite catalyst particle, showing that the optimized catalyst can be many times more active. In addition, a well-designed pore network is also beneficial to improving catalyst lifetime. For example, the useful lifetime of a hydrodemetalation catalyst can be doubled by numerically optimizing the hierarchical pore network[8]. Meanwhile, many experimental techniques have been developed to synthesize calculated optimal pore structures[9–11].

In the aforementioned works, the optimization of the catalyst pore network structure ignores possible effects of deactivation by coking. No studies that include this effect have been reported, to the best of our knowledge, although deactivation by coke formation is commonplace in numerous industrial processes, e.g., fluid catalytic cracking[12,13], catalytic reforming of methane[12,14], and propane dehydrogenation[15].

In catalyst particles, the process of catalyst deactivation by coking can be very complex. Coke is regarded as an undesired byproduct, and the types of coke formed in catalysts can be largely different. The composition of coke includes aliphatics, aromatics, and pregraphite, and the formation of coke could involve several active sites and many reactions[16]. At the catalyst particle level, coke deactivates catalysts following three mechanisms, namely, site coverage, pore narrowing, and pore blockage[12,17,18] (see the illustrations in Figure S1 in the Supplementary Information). Firstly, coke covers catalytic active sites and isolates these sites from reactants. Secondly, coke often covers the internal surface non-uniformly at the catalyst particle level,

because of the significant concentration gradients of coke precursors in the particle. Then, with the buildup of coke on the pore surface, coke narrows the pores and thus adds diffusion resistance, which further reduces the activity of the catalyst particles. Finally, coke can even plug pores, leading to the complete deactivation of these pores. When the fraction of open pores drops below a critical threshold, namely, the percolation threshold, the previously connected, particle-spanning cluster of open pores becomes disconnected and many open pores become inaccessible to reactants[19–22]. This percolation phenomenon can lead to a large change in macroscopic properties, like the effective diffusivities of the components and the observed reaction rates[20,21]. As a result, the catalyst pore network structure could have an important effect on the process of deactivation by coking, and, in turn, coking changes the pore network structure with time. Considering these interrelated phenomena, the optimization of the catalyst pore network structure in the presence of deactivation by coking should be performed, aided by a proper mathematical model.

Continuum models are commonly employed to perform the optimization of catalyst pore network structures in the absence of deactivation by coking. Continuum models are characterized by a pseudo-homogeneous description of diffusivity, reaction rate, tortuosity, and many other macroscopic properties at length scales much larger than the dimension of individual pores[19–21]. Due to this pseudo-homogeneous assumption, continuum models are simple and efficient, provided that the pore network structure does not change significantly. However, the process of deactivation by coking is usually accompanied by significant changes in pore network

structure, and the percolation threshold could even be reached, in which case continuum models break down[23].

A discrete model is an appropriate alternative to optimize catalyst pore network structure in the presence of deactivation by coking. Common types of discrete models include Bethe lattices[24,25] and various pore network models[24,26] to describe both morphology and topology of the void space in catalyst particles, and thus the local heterogeneity and dynamic change in pore network structure can be properly accounted for. More importantly, pore network models have been successfully used to simulate some reaction systems with percolation phenomena, such as hydrodesulphurization[27,28], hydrodemetalation[1,19,20], deactivation of immobilized glucose isomerase[29–31], benzene hydrogenation[32,33], and propane dehydrogenation[34]. Therefore, a pore network model is preferable to carry out the optimizations in this work.

Propane dehydrogenation is an appropriate model reaction system for investigation, because of its industrial and academic importance. At present, propane dehydrogenation is one of the most important methods for the on-purpose production of propene, a key feedstock in the petrochemical industry[15,35–37]. Although this process has been commercialized, its catalysts are still plagued by deactivation due to coking. For example, the Pt-Sn/$ZnAl_2O_4$ catalyst used in the Uhde STAR process should be regenerated after 7 hours on stream; the CrO_x/Al_2O_3 catalyst used in the Catofin process is significantly deactivated after only 12 minutes[38,39]. Recently, we proposed a two-dimensional pore network model to simulate the process of deactivation by coking in a Pt-Sn/Al_2O_3 particle for non-oxidative propane dehydrogenation, and we found that the pore network structure strongly affects this deactivation process and the catalyst

performance[34]. However, to the best of our knowledge, no literature has reported the optimization of propane dehydrogenation catalyst particles even in the absence of deactivation by coking, let alone in its presence.

In this work, a three-dimensional pore network model is proposed, and employed to optimize the catalyst pore network structure in the presence of deactivation by coking. Non-oxidative propane dehydrogenation in a Pt-Sn/Al_2O_3 catalyst particle is taken as the model reaction system. Generally, catalyst particles could contain a unimodal or a bimodal pore network[40,41]; thus, optimizations for both types of networks are presented here. For unimodal pore networks, the porosity, pore connectivity, pore size, and their spatial distributions are optimized; for bimodal pore networks, the arrangement, porosity, and radius of the broad pores are optimized. This work presents a powerful pore network model and some useful guidance for developing catalyst particles with high resistance against deactivation by coking.

Modeling Approach

The three-dimensional pore network model used for optimization can be divided into three parts, namely, the pore network, the modeling equations for reaction and diffusion, and those for coking and deactivation. These parts are intimately coupled: the pore network provides the surface area and pore volume for diffusion, reaction, coking, and deactivation; solving the equations for reaction and diffusion yields the concentration profiles of reactants and products, which determine the rates of coking and deactivation; the solution of the coking and deactivation equations are used to update the pore network structure and the distribution of catalytic activity, which, in turn, affects reaction and diffusion.

Before introducing the three parts of the pore network model, the following assumptions are made: Pt-Sn/Al_2O_3 is chosen as the model catalyst, since it is widely used in propane dehydrogenation processes[15]; the gradients of temperature and total pressure are assumed to be negligible, which has been proven in the literature[34]; side reactions, except for the coke formation reaction, can be neglected under the reaction conditions in this work[15]; coke is assumed to be non-catalytic and its formation is irreversible[45]; all types of coke are assumed to have similar properties and they deactivate the catalyst particle following the same mechanisms[45]. For all the catalyst particles, either the intrinsic activity per unit catalyst weight is assumed to be constant, or the intrinsic activity per unit internal surface area is assumed to be the same. These two distinct assumptions about the intrinsic activity are compared, because different assumptions can lead to different optimization results. In practice, the two assumptions about the intrinsic activity are reasonable to a large extent: the metal loading per unit catalyst weight stays constant when the incipient wetness impregnation method is used; the metal loading per unit internal surface area tends to be constant when the wet impregnation method is adopted[42]. In this work, only the primary features and principal model equations of the three-dimensional pore network model are described, since the model is similar to the two-dimensional one in our previous work, where more details can be found[34].

Pore network

The three-dimensional pore network within a spherical domain (see Figure 1) is used to describe the pore space of a spherical catalyst particle; the method of generating this pore

network is adopted from the literature, where its details can be found[43]. The nodes and bonds are assumed to be zero-volume intersections and cylindrical pores, respectively. These pores are connected to their neighbors, according to a predefined connectivity. Their pore radii are deliberately assigned to achieve unimodal and bimodal pore size distributions, as well as various spatial distributions of pore size. It is worth noting that the external shape of a catalyst particle can affect the catalyst performance to some extent[43]. However, this work focuses on optimizing the pore network structure inside the catalyst particle, and the external shape would not qualitatively affect these optimization results or the general conclusions.

The statistical pore volume distribution of unimodal pore networks is assumed to follow a log-normal distribution:

$$f\left(r_o\right)=\frac{V_t}{\sqrt{2\pi}r_o\sigma}\exp\left[-\frac{\left(\ln r_o-\ln r_a\right)^2}{2\sigma^2}\right] \quad (1),$$

where r_o and r_a are the original (initial) and volume-averaged pore radii for a fresh catalyst particle, σ is the standard deviation of the natural logarithm of the pore radius, and V_t is the total pore volume of the catalyst particle. Three characteristic spatial distributions of pore size are compared in this work. They are the random, uniform spatial distribution of pore size (UD1), the descending distribution of pore size toward the center of the catalyst particles (UD2), and the ascending distribution of pore size toward the center of the catalyst particles (UD3). The three spatial distributions of pore size are illustrated in Figure 2a, while the method of generating these distributions can be found elsewhere[44].

Bimodal pore networks contain both narrow and broad pores. A bimodal pore network is generated by performing the following two steps: firstly, according to the log-normal distribution (see Eq. 1), randomly assigning a narrow pore radius to each pore in the network; then, replacing some narrow pores with broad pores that have a uniform pore radius. Two characteristic spatial distributions of broad pores are investigated in this work, which are illustrated in Figure 2b: a random, uniform spatial distribution of broad pores (BD1), and a spatial distribution where all broad pores form a cluster that is directly connected to the outer surface of the catalyst particle (BD2).

Equations describing reaction and diffusion

The process of the main reaction (here, propane dehydrogenation to propene) and diffusion can be described by the following principal equations in the cylindrical pores and nodes. In a cylindrical pore, the quasi-steady-state condition is satisfied, as the rates of the main reaction and diffusion are much faster than the rate of coke formation[15], and the steady-state continuity equation for component *i* is:

$$\frac{dJ_i}{dl} - \frac{2r_o R_i}{r^2} = 0 \qquad (2),$$

where r and l are the radius and length of the pore, R_i is the reaction rate of component i per unit pore surface area, and J_i is the diffusion flux of component i.

The equation for R_i is taken from the work by Li et al.[45]:

$$R_i = a\,v_i \frac{k_1\left(P_{C_3H_8} - P_{C_3H_6}P_{H_2}/K\right)}{S_{cat}\left(1 + K_2 P_{C_3H_6} + K_3^{0.5} P_{H_2}^{0.5}\right)^2} \qquad (3),$$

where a ($0 \le a \le 1$) is the deactivation function for the main reaction (see Eqs. 11 and 12), v_i is the stoichiometric number of component i, S_{cat} is the internal specific surface area of a catalyst particle, k_1 and K are the reaction rate and reaction equilibrium constants, K_2 and K_3 are the adsorption equilibrium constants, and $P_{C_3H_8}$, $P_{C_3H_6}$, and P_{H_2} are the partial pressures of propane, propene, and hydrogen, respectively. The temperature-dependent equations for the kinetic parameters (k_1, K, K_2, and K_3) in Eq. 3 are also adopted from the same literature[45].

The equation for J_i follows Fick's law:

$$J_i = -D_{i,e}\frac{dC_i}{dl} \quad (4),$$

where C_i is the concentration of component i and $D_{i,e}$ is the effective diffusivity of component i. $D_{i,e}$ is determined by a modified Wilke-Bosanquet equation[1,8,46]:

$$D_{i,e} = \left(1-\frac{r}{r_o}\right)^4 \frac{D_{i,M}D_{i,K}}{D_{i,M}+D_{i,K}} \quad (5),$$

$$D_{i,M} = \frac{1-x_i}{\sum_{\substack{j=1\\ j\neq i}}^{n}\frac{x_j}{D_{i,j}}} \quad (6),$$

where $D_{i,K}$ is the Knudsen diffusivity of component i that is calculated by using the kinetic theory of gases[47], $D_{i,j}$ is the binary diffusivity of component i in a mixture of i and j that is obtained from the Chapman-Enskog equation[48], and x_i and x_j are the mole fractions of component i and j. This modified Wilke-Bosanquet equation includes the effect of pore narrowing caused by coke deposition, which can lead to restricted, "configurational" diffusion[8,46]. It should be noted that the Wilke-Bosanquet model is adequate because the results

calculated by this model are almost the same as the ones obtained from the more complex and also more computationally intensive Dusty Gas model, as shown in our previous work[34].

For an inner node, Kirchhoff's law is satisfied, due to its zero-volume assumption:

$$\sum_{n=1}^{n=Z} \pi r_n^2 J_{i,n} = 0 \quad (7),$$

where Z is the pore connectivity, r_n is the radius of pore n, and $J_{i,n}$ is the diffusion flux of component i in pore n. For a boundary node, a Dirichlet boundary condition is used:

$$C_i = C_{i,b} \quad (8),$$

where $C_{i,b}$ is the bulk concentration of component i.

Equations describing coking and deactivation

The process of coking and deactivation in cylindrical pores is described by the following equations. The accumulation of coke over time in a cylindrical pore can be described by:

$$C_c(t + \Delta t) = C_c(t) + R_c(t)\Delta t \quad (9),$$

where $C_c(t)$ (with $C_c(0) = 0$ g/m^2) is the loading of coke in a pore at time t, Δt is the time step, and R_c is the coking rate per unit pore surface area. R_c is calculated by the coking kinetics reported in the literature[45]:

$$R_c = \frac{dC_c}{dt} = a_c \frac{k_c P_{C_3H_6}}{1 + K_3 P_{H_2}} \quad (10),$$

where a_c is the deactivation function for the coke formation reaction (see Eqs. 11 and 12) and k_c is the reaction rate constant of the coke formation reaction.

Coke deactivates a catalyst particle in three ways: site coverage, pore narrowing, and pore blockage[12,34] (see the illustrations in Figure S1 in the Supplementary Information). The contribution of site coverage to catalyst deactivation is reflected by the deactivation functions (a and a_c) in Eqs. 3 and 10. In this work, we assume that the coke formation reaction and main reaction occur on the same sites and a single site is involved in the rate-determining steps of these reactions. Based on this assumption, the deactivation functions can be described by[18]:

$$a = a_c = \frac{C_{cm} - C_c}{C_{cm}} \tag{11},$$

where C_{cm} is the maximum loading of coke required to completely deactivate the active sites on the catalyst surface. Equation 11 is a good approximation to calculate the activity loss caused by site coverage, as has been proven in the literature[45]. When combining Eqs. 10 and 11, we obtain:

$$-\frac{da}{dt} = a\frac{k_d P_{C_3H_6}}{1 + K_3 P_{H_2}} \quad k_d = \frac{k_c}{C_{cm}} \tag{12},$$

where k_d is the deactivation rate constant, which is a temperature-dependent function that can be adopted from the literature[45].

The contribution of pore narrowing to catalyst deactivation is reflected in Eq. 5, where the additional diffusion resistance caused by pore narrowing is included. In Eq. 5, the real-time pore radius of a cylindrical pore (r) can be obtained from the coke loading (C_c)[46]:

$$r = \sqrt{r_o^2 - 2C_c r_o / \rho_c} \tag{13},$$

where ρ_c is the coke density.

The contribution of pore blockage to catalyst deactivation is also important. When the real-time radius of a pore is smaller than the molecular radius of propane (0.215 nm)[49], this pore is regarded as plugged by coke and completely deactivated. Some open pores could be surrounded by plugged pores and then become inaccessible to reactants, and such pores are also completely deactivated. In this case, the extended Hoshen-Kopelman algorithm[50] is employed to identify these inaccessible pores.

Optimization

The objective function is the time-averaged propene formation rate per unit catalyst volume (R_{obj}), which reflects both activity and stability of a catalyst particle, as illustrated in Figure 3:

$$R_{obj} = \frac{\int_{t=0}^{t=t_m} R_{app} dt}{t_m} \tag{14},$$

where t_m is the maximum time for reaction and R_{app} is the apparent reaction rate for propene formation (mol/m^3/s). R_{app} can be determined by using a scaling rule[1,24]:

$$R_{app} = R_{PN} \cdot f = \sum_{n=1}^{N} \left(2\pi r_{o,n} l_n R_{C_3H_6,n} \right) \cdot \frac{\varepsilon}{\sum_{n=1}^{N} \left(\pi r_{o,n}^2 l_n \right)} \tag{15},$$

where R_{PN} is the overall reaction rate in a pore network, f is the scaling factor, $R_{C_3H_6,n}$ is the formation rate of propene in pore n, and ε is the porosity of a catalyst particle. $R_{C_3H_6,n}$ is obtained by solving the pore network model, and the algorithm for this model can be found in our previous work[34]. The simulations are performed in MATLAB 2016b.

For unimodal pore networks, three spatial distributions of pore size (i.e., UD1, UD2, and UD3, see Figure 2a) are compared; the porosity, the pore connectivity, the volume-averaged pore radius, and the standard deviation are optimized. For bimodal pore networks, two spatial distributions of broad pores (i.e., BD1 and BD2, see Figure 2b) are compared; the porosity and radius of the broad pores are optimized.

Results and Discussion

A typical simulation

Before optimizing the catalyst pore network structure, a typical simulation is conducted to obtain the fundamental characteristics of deactivation by coking in a catalyst particle and also to provide a benchmark for comparison in the following sections. The catalyst particle for this typical simulation contains a unimodal pore network with randomly distributed pore size (i.e., UD1). The simulation parameters are given in Table 1. The number of nodes, 2139, is adequate to obtain accurate simulation results (see Figure S2 in the Supplementary Information), while adding more nodes would increase computational cost significantly. The time step, 250 s, is also reasonable, as proven in Figure S3. Besides, the pore size distribution of this benchmark catalyst particle is very close to that of a commercial Pt-Sn/Al_2O_3 catalyst[51], and other structural parameters are typical for Al_2O_3 particles. The simulation results are presented in Figs. 3 and 4.

Figure 3 shows the change over time in the apparent reaction rate for propene formation. The apparent reaction rate decreases from 8.40 mol/m^3/s to only 0.36 mol/m^3/s after 10000 s on

stream. This decrease in activity can be attributed to the deposition of coke, which covers active sites, narrows pores, and even plugs pores. Figure 3 also illustrates the definition of the time-averaged propene formation rate (R_{obj}), which is the objective function in this work. For the catalyst particle in this typical simulation, R_{obj} is 1.90 mol/m^3/s, which is considered as the benchmark for comparison. To gain more insight into the process of deactivation by coking, the distributions of coke-plugged pores and concentrations of propane at different reaction times (t = 250, 2000, and 4000 s) are given in Figure 4.

In Figure 4a, when $t \leq 2000$ s, many pores in the central zone of the catalyst particle are still accessible to the reactant and products; when $t \geq 4000$ s, the plugged and inaccessible pores form a large cluster that occupies the central zone of the catalyst particle. As observed in Figure 4b, the concentration gradient of propane at t = 250 s is very steep, indicating strong diffusion resistance. With the progression of coke deposition, pores get narrower and the diffusion resistance increases. When $t \geq 4000$ s, only the pores in the outer zone of the catalyst particle are available for propane dehydrogenation, while the central zone is completely deactivated.

Unimodal pore network

Figure 5 shows the effect of porosity (ε) on the time-averaged propene formation rate (R_{obj}) of the catalyst particles with three different initial spatial distributions of pore size (i.e., UD1, UD2, and UD3, see Figure 2a). For the same porosity, R_{obj} for UD2 is the highest, while the one for UD3 is the lowest (< 0.10 mol/m^3/s). For UD2, the large pores are located in the outer zone of the catalyst particle, and this spatial distribution is favorable in two aspects. Firstly, this

decreases the diffusion resistance in the outer zone, which is the primary zone for the propane dehydrogenation reaction; secondly, the large open pores do not tend to become inaccessible during the coking process, as they are not surrounded by small pores. For the effect of spatial distributions of pore size, similar results are observed in Figs. 6-8, which can be explained in the same way.

In Figure 5a, the optimal porosity for UD1 is 0.5 and the corresponding R_{obj} is 1.91 mol/m^3/s; the optimal porosity for UD2 is 0.4 and its R_{obj} is 5.69 mol/m^3/s, which is 200% higher than the benchmark (1.90 mol/m^3/s, see Table 1 for the corresponding pore network structure). Under the assumption of constant intrinsic activity per unit catalyst weight, these results in Figure 5a can be explained by a compensation effect where, on the one hand, a high porosity indicates more void space for diffusion and thus is more favorable for diffusion, while, on the other hand, a high porosity also means less catalyst weight for reaction. In Figure 5b, R_{obj} for UD1 and UD2 increase almost linearly with porosity. Under the assumption of constant intrinsic activity per unit internal surface area, a high porosity indicates high diffusion flux and also large catalyst surface area for reaction, which leads to the increased R_{obj} in Figure 5b. The linear increase of R_{obj} in Figure 5b can also be explained based on Eq. 15. The overall reaction rate in a pore network (R_{PN}) in Eq. 15 does not change with porosity under this assumption of intrinsic activity, but the scaling factor (f) increases linearly with porosity. Therefore, a porosity close to 1 would be optimal, but due to the limited mechanical stability of the catalyst particles in a tubular reactor, one has to fix the total porosity to a smaller value, for example, 0.6-0.7.

Figure 6 displays the effect of pore connectivity (Z) on R_{obj} of the catalyst particles with UD1, UD2, and UD3 spatial distributions. For UD1 and UD2, R_{obj} slightly increases with Z changing from 4 to 6, and then fluctuates slightly, which is purely due to statistical effects, as noted from repeated simulations for several statistical realizations of the pore network (see Figure S4 in the Supplementary Information). A higher pore connectivity leads to weaker diffusion resistance, and large pores are less likely to be surrounded by the coke-plugged pores. However, these favorable effects are negligible when pore connectivity is large enough ($Z \geq 6$, in this case). Generally, R_{obj} is not sensitive to pore connectivity ($Z \geq 4$) in this reaction system, and a connectivity of 6 is adequate.

In Figure 7a, R_{obj} increases significantly when the volume-averaged pore radius (r_a) changes from 3.5 to around 50 nm for all three spatial distributions, after which R_{obj} increases more slowly to an asymptotic value at $r_a > 250$ nm. Remarkably, when $r_a = 250$ nm, R_{obj} for UD1 and UD2 reaches 20.72 and 27.45 mol/m^3/s, respectively, which is 10.9 and 14.4 times larger than the benchmark (1.90 mol/m^3/s). Under the assumption of constant intrinsic activity per unit catalyst weight, a large r_a is favorable to enhance R_{obj} in two ways: firstly, the diffusion resistance decreases significantly, as Knudsen diffusion is dominant in the range of 3.5 nm $\leq r_a \leq$ 50 nm and it is still important in the range of 50 nm $\leq r_a \leq$ 250 nm (see Figure S5 in the Supplementary Information); secondly, large pores are more resistant to deactivation caused by pore narrowing and pore blockage. In Figure 7b, the optimal r_a for UD1 and UD2 is 20 and 9 nm, respectively, and the corresponding R_{obj} is 3.87 and 7.56 mol/m^3/s, which is about 2 and 4 times

larger than the benchmark (1.90 mol/m^3/s). When the intrinsic activity per unit internal surface area is assumed to be constant, there exists a compensation effect where, on the one hand, a large pore radius is more beneficial for diffusion, while, on the other hand, a large pore radius also indicates less pores when porosity is fixed, and thus a lower internal surface area for reaction. This compensation effect explains the results for UD1 and UD2 in Figure 7b. For UD3, the optimal r_a (50 nm) is much larger than the optimum for UD1 and UD2, as the diffusion resistance is more severe and, therefore, a larger r_a is required to reach the maximum R_{obj} (1.53 mol/m^3/s). Besides, when r_a is large enough, the diffusion limitations become negligible and the spatial distribution of the pores would have no effect on the result, as shown by the convergence of R_{obj} for UD1, UD2, and UD3 to the same values at $r_a \geq 250$ nm (see Figure 7b).

Moving to the effect of the standard deviation (σ), in Figure 8, for $\sigma = 0$, all the pores in the pore network have the same radius (i.e., 5 nm) and R_{obj} is the same for the three spatial distributions. For UD1, R_{obj} decreases when σ increases from 0 to 1. A large σ indicates a broad pore size distribution. Due to this, large pores are more likely to be surrounded by small pores and become inaccessible during the coking process, which has a strong detrimental effect on the apparent activity. Comparing, as before, the assumptions of constant intrinsic activity per unit weight (a) and per unit surface area (b), for UD2, there exists a maximum R_{obj} (5.68 mol/m^3/s) at $\sigma = 0.5$ in Figure 8a and a maximum R_{obj} (6.44 mol/m^3/s) at $\sigma = 0.7$ in Figure 8b. This is because of a compensation effect. On the one hand, a broader pore size distribution means that larger pores are located in the outer zone of the catalyst particle, which enhances the apparent activity;

on the other hand, a broader pore size distribution also indicates that smaller pores are located in the central zone, which makes the central zone almost useless for reaction. For UD3, R_{obj} decreases when σ increases from 0 to 1. The outer zone of the catalyst particle is the primary zone for the propane dehydrogenation reaction, because it is exposed to the environment. Thus, placing smaller pores in the outer zone results in a lower R_{obj}.

Bimodal pore network

For the bimodal catalysts, the porosity corresponding to narrow pores (ε_N) is assumed to be 0.45, and the porosity associated to broad pores (ε_B) varies with the number of broad pores in the pore network. The total porosity (ε) can be calculated by:

$$\varepsilon = \varepsilon_B + (1-\varepsilon_B)\varepsilon_N \tag{16}$$

Figure 9 shows the effect of total porosity (ε) on R_{obj} in catalyst particles with spatial distributions of broad pores of types BD1 and BD2. R_{obj} for BD2 is larger than the one for BD1. For example, in Figure 9a, R_{obj} for BD2 (4.13 mol/m^3/s) is 2.4 times as large as for BD1 (1.73 mol/m^3/s) at ε = 0.70; in Figure 9b, R_{obj} for BD2 (4.95 mol/m^3/s) is 2.5 times as large as for BD1 (2.01 mol/m^3/s) at ε = 0.70. If broad pores are randomly distributed in the pore network (BD1), these broad pores are more likely to be surrounded by narrow pores and easily become inaccessible to reactant during the coking process. However, if broad pores form a large cluster that is directly connected to the outer surface (BD2), these broad pores remain accessible, as long as they are not plugged by coke. This explains the higher R_{obj} for BD2. For the effect of the spatial distribution of the broad pores, similar results are found in Figure 10, which can be explained in the same way.

As seen from Figure 9a, there exists a maximum R_{obj} for BD2 (4.49 mol/m^3/s) at a total porosity of 0.78. This optimal bimodal catalyst particle is 2.4 times more active and uses 60% less catalyst weight, when compared to the unimodal benchmark catalyst (see Table 1 for its pore network structure). Under the assumption of constant intrinsic activity per unit catalyst weight, more broad pores in BD2 indicate lower diffusion resistance and higher resistance against deactivation caused by pore blockage, but less catalyst weight for reactions. The two competing factors lead to the optimal total porosity for BD2. In Figure 9b, the R_{obj} for BD2 increases with the total porosity. Under the assumption of constant intrinsic activity per unit internal surface area, more broad pores indicate lower diffusion resistance, higher resistance against deactivation caused by pore blockage, and larger internal surface area for reactions, which result in the increased R_{obj} for BD2. In practice, the BD2 spatial distribution of broad pores is preferable for bimodal catalysts, while the preferable total porosity should be a compromise between apparent activity and crush strength. This archetype in spatial distribution is also expected to be closer in nature to the one formed during catalyst pellet synthesis from smaller particles.

Figure 10 displays the effect of the broad pore radius (r_B) on R_{obj} in the catalyst particles at the fixed total porosity of 0.70. For BD2, there exist a maximum R_{obj} (4.28 mol/m^3/s) at r_B = 18 nm in Figure 10a and a maximum R_{obj} (5.35 mol/m^3/s) at r_B = 15 nm in Figure 10b. As the total porosity is fixed in this case, a larger r_B indicates weaker diffusion resistance in the cluster of broad pores, on the one hand, and also a smaller number of broad pores in the cluster, on the other hand. The two competing factors lead to an optimal r_B. For BD1, R_{obj} decreases when r_B

increases from 10 to 150 nm. When r_B is large and the number of broad pores is small, these broad pores are easily surrounded by coke-plugged narrow pores and, then, become inaccessible to the reactant, thus become completely deactivated. In Figure 10a, the bimodal catalyst particle with spatial distribution BD2 and an optimal broad pore radius of 18 nm is 2.3 times more active and saves 45% catalyst weight, when compared to the unimodal benchmark catalyst. In Figure 10b, the optimal bimodal catalyst particle is 2.8 times more active and saves 45% catalyst weight when compared to the benchmark catalyst.

It should be noted that the BD2 adopted in this work are subsets of the universal set containing all BD2, and they are not the globally optimal spatial distribution of broad pores, as the broad pores are concentrated locally. Using continuum models and assuming negligible pore blockage, Coppens and coworkers[8,40,53,54] found that BD2, with broad pores uniformly distributed, is very close to the optimal distribution, even when deactivation occurs in a catalyst particle. When simulating the catalyst particle with this close-to-optimal BD2 by using the pore network model in this work, the scaling rule (Eq. 15) breaks down, since the concentration profiles of reactants and products vary significantly with the dimension (or the number of pores) of the pore network. In this case, to assure the accuracy of the simulation, a pore network with the real number of pores (~10^{16}, if the pore length approximates the pore diameter of the narrow pores) should, ideally, be used. Such simulation would be too computationally expensive to perform on any computer. To solve this problem, a multi-scale pore network model should be proposed, which will be the subject of future work.

Conclusions

The pore network structure of a Pt-Sn/Al_2O_3 catalyst particle for propane dehydrogenation is optimized by using a three-dimensional pore network model, and accounting for significant deactivation by coking over time. The model describes coupled diffusion, reaction, coking, and deactivation; it also includes three mechanisms of deactivation by coking, namely, site coverage, pore narrowing, and pore blockage, and it assumes all types of coke deactivate the catalyst particle following the above three mechanisms. A time-averaged propene formation rate is defined as the objective function for optimization, which reflects both apparent activity and stability of the catalyst particle. Unimodal and bimodal pore networks are optimized under two separate assumptions, namely, constant intrinsic activity per unit catalyst weight and constant intrinsic activity per unit internal surface area.

For a unimodal catalyst particle, placing large pores in the outer zone of catalyst particles (UD2) is the favorable spatial distribution, due to the improved diffusion in the outer zone and weakened effect of pore blockage. Under the assumption of constant intrinsic activity per unit catalyst weight, there exists an optimal porosity (e.g., 0.4 for UD2), a pore connectivity of 6 is adequate, a large volume-averaged pore radius is preferred, and there is an optimal width of the pore size distribution (σ = 0.5) for UD2. Under the assumption of constant intrinsic activity per unit internal surface area, a large porosity is favorable, a pore connectivity of 6 is adequate, there is an optimal volume-averaged pore radius (9 nm) for UD2, and there exists an optimal width of the pore size distribution (σ = 0.7) for UD2. For a bimodal catalyst particle, connecting broad

pores into a cluster directly exposed to the external surface (BD2) is more favorable than randomly distributing these broad pores (BD1), because the effect of pore blockage is much weaker for BD2. This implies a truly hierarchical pore size distribution, with large pore channels interspersed by narrow ones. Under the assumption of constant intrinsic activity per unit catalyst weight, there exist an optimal total porosity (ε = 0.78) and an optimal broad pore radius (r_B = 18 nm) for BD2. Under the assumption of constant intrinsic activity per unit internal surface area, a large total porosity is favorable and there exists an optimal broad pore radius (r_B = 15 nm) for BD2. The optimized unimodal catalyst particle with the UD2 spatial distribution of pore size and a volume-averaged pore radius of 250 nm can be up to 14 times more active than the benchmark, which indicates that engineering the catalyst pore network structure is a very effective approach to improve the performance of industrial catalyst particles for propane dehydrogenation.

This article has presented a three-dimensional pore network model and some useful guidelines for optimizing catalyst particles in the presence of deactivation by coke formation, which could be applied to other processes as well. It should also be noted that the BD2 in this work are subsets of the universal set containing all BD2. To find the globally optimal BD2, a multi-scale pore network model should be developed, which is one of our objectives for future work.

Acknowledgments

This work was supported by the National Natural Science Foundation of China (21706067 and U1663221), the China Postdoctoral Science Foundation (2018T110358), the “Chenguang Program” supported by Shanghai Education Development Foundation and Shanghai Municipal

Education Commission (17CG29), and the Fundamental Research Funds for the Central Universities (222201714004 and 222201718003). M.-O.C is supported by an EPSRC "Frontier Engineering" grant for the UCL Centre for Nature Inspired Engineering (EP/K038656/1), and the UK Catalysis Hub (EP/K014706/1).

Notation

C_c loading of coke, g/m^2

C_{cm} maximum loading of coke, g/m^2

C_i concentration of component *i*, mol/m^3

$C_{i,b}$ bulk concentration of component *i*, mol/m^3

$D_{i,e}$ effective diffusivity of component *i*, m^2/s

J_i diffusion flux of component *i*, mol/m^2/s

$J_{i,n}$ diffusion flux of component *i* in pore *n*, mol/m^2/s

l pore length, m

l_n length of pore *n*, m

P_i partial pressure of component *i*, bar

$P_{i,b}$ bulk partial pressure of component *i*, bar

r pore radius, m

r_n radius of pore *n*, m

r_a, r_o original and volume-averaged pore radii for a fresh catalyst particle, m

R_c coking rate per unit pore surface area, g/m^2/s

R_i reaction rate per pore surface area of component *i*, mol/m^2/s

S_{cat} surface area for a fresh catalyst particle, m^2/g

t time, s

x_i mole fraction of component *i*, dimensionless

Z pore network connectivity, dimensionless

σ standard deviation, dimensionless

ρ_c coke density, g/m^3

ε total porosity, dimensionless

References

1. Keil FJ, Rieckmann C. Optimization of three-dimensional catalyst pore structures. *Chem Eng Sci*. 1994;49:4811-4822.
2. Hegedus LL, Pereira CJ. Reaction engineering for catalyst design. *Chem Eng Sci*. 1990;45:2027-2044.
3. Beeckman JW, Hegedus LL. Design of monolith catalysts for power plant NO_x emission control. *Ind Eng Chem Res*. 1991;30:969-978.
4. Keil FJ, Rieckmann C. Optimization of catalyst pore structures. *Hungarian J Ind Chem*. 1993;21:277-286.
5. Wang G, Coppens MO. Calculation of the optimal macropore size in nanoporous catalysts and its application to $DeNO_x$ catalysis. *Ind Eng Chem Res*. 2008;47:3847-3855.

6. Wang G, Coppens M-O. Rational design of hierarchically structured porous catalysts for autothermal reforming of methane. *Chem Eng Sci*. 2010;65:2344-2351.

7. Wei J. Catalyst designs to enhance diffusivity and performance-I: Concepts and analysis. *Chem Eng Sci*. 2011;66:4382-4388.

8. Rao SM, Coppens M. Increasing robustness against deactivation of nanoporous catalysts by introducing an optimized hierarchical pore network- Application to hydrodemetalation. *Chem Eng Sci*. 2012;83:66-76.

9. Soler-lllia GJ de AA, Sanchez C, Lebeau B, Patarin J. Chemical strategies to design textured materials: from microporous and mesoporous oxides to nanonetworks and hierarchical structures. *Chem Rev*. 2002;102:4093-4138.

10. Hartmann S, Brandhuber D, Hüsing N. Glycol-Modified silanes: Novel possibilities for the synthesis of hierarchically organized (hybrid) porous materials. *Acc Chem Res*. 2007;40:885-894.

11. Huczko A. Template-based synthesis of nanomaterials. *Appl Phys A*. 2000;70:365-376.

12. Froment GF. Kinetic modeling of hydrocarbon processing and the effect of catalyst deactivation by coke formation. *Catal Rev*. 2008;50:1-18.

13. Vogt ETC, Weckhuysen BM. Fluid catalytic cracking: Recent developments on the grand old lady of zeolite catalysis. *Chem Soc Rev*. 2015;44:7342-7370.

14. Pakhare D, Spivey J. A review of dry (CO_2) reforming of methane over noble metal catalysts. *Chem Soc Rev*. 2014;43:7813-7837.

15. Sattler JJHB, Ruiz-Martinez J, Santillan-Jimenez E, Weckhuysen BM. Catalytic dehydrogenation of light alkanes on metals and metal oxides. *Chem Rev*. 2014;114:10613-10653.

16. Wang H-Z, Sun L-L, Sui Z-J, et al. Coke formation on Pt–Sn/Al_2O_3 catalyst for propane dehydrogenation. *Ind Eng Chem Res*. 2018;57:8647-8654.

17. Froment GF. Coke formation in catalytic processes: Kinetics and catalyst deactivation. *Stud Surf Sci Catal*. 1997;111:53-68.

18. Froment GF. Modeling of catalyst deactivation. *Appl Catal A Gen*. 2001;212:117-128.

19. Arbabi S, Sahimi M. Computer simulations of catalyst deactivation-II. The effect of morphological, transport and kinetic parameters on the performance of the catalyst. *Chem Eng Sci*. 1991;46:1749-1755.

20. Arbabi S, Sahimi M. Computer simulations of catalyst deactivation-I. Model formulation and validation. *Chem Eng Sci*. 1991;46:1739-1747.

21. Sahimi M, Gavalas GR, Tsotsis TT. Statistical and continuum models of fluid-solid reactions in porous media. *Chem Eng Sci*. 1990;45:1443-1502.

22. Stauffer D. *Introduction to Percolation Theory*. London: Taylor and Francis; 1985.

23. Zhang L, Seaton NA. The application of continuum equations to diffusion and reaction in pore networks. *Chem Eng Sci*. 1994;49:41-50.

24. Keil F. Diffusion and reaction in porous networks. *Catal Today*. 1999;53:245-258.

25. Beeckman J, Froment G. Catalyst deactivation by active site coverage and pore blockage. *Ind Eng Chem Fundam*. 1979;18:245-256.

26. Hollewand MP, Gladden LF. Representation of porous catalysts using random pore networks. *Chem Eng Sci*. 1992;47:2757-2762.

27. Wood J, Gladden LF. Modelling diffusion and reaction accompanied by capillary condensation using three-dimensional pore networks. Part 1. Fickian diffusion and pseudo-first-order reaction kinetics. *Chem Eng Sci*. 2002;57:3033-3045.

28. Wood J, Gladden LF, Keil FJ. Modelling diffusion and reaction accompanied by capillary condensation using three-dimensional pore networks.Part 2. Dusty gas model and general reaction kinetics. *Chem Eng Sci*. 2002;57:3047-3059.

29. Dadvar M, Sahimi M. Pore network model of deactivation of immobilized glucose isomerase in packed-bed reactors II: Three-dimensional simulation at the particle level. *Chem Eng Sci*. 2002;57:939–952.

30. Dadvar M, Sahimi M. Pore network model of deactivation of immobilized glucose isomerase in packed-bed reactors. Part III: Multiscale modelling. *Chem Eng Sci*. 2003;58:4935-4951.

31. Dadvar M, Sohrabi M, Sahimi M. Pore network model of deactivation of immobilized glucose isomerase in packed-bed reactors. I: Two-dimensional simulations at the particle level. *Chem Eng Sci*. 2001;56:2803-2819.

32. Ye G, Zhou X, Coppens M-O, Yuan W. Probing pore blocking effects on multiphase reactions within porous catalyst particles using a discrete model. *AIChE J*. 2016;62:451-460.

33. Ye G, Zhou X, Coppens M-O, Zhou J, Yuan W. Influence of catalyst pore network structure on the hysteresis of multiphase reactions. *AIChE J*. 2017;63:78-86.

34. Ye G, Wang H, Duan X, Sui Z, Zhou X, Coppens M-O, Yuan W. Pore network modeling of catalyst deactivation by coking, from single site to particle, during propane dehydrogenation. *AIChE J*. 2019;65:140-150.

35. Galvis Hirsa MT, de Jong KP. Catalysts for production of lower olefins from synthesis gas: A review. *ACS Catal*. 2013;3:2130-2149.

36. Corma A, Melo F V, Sauvanaud L, Ortega F. Light cracked naphtha processing : Controlling chemistry for maximum propylene production. *Catal Today*. 2005;107-108:699-706.

37. Carrero CA, Schloegl R, Wachs IE, Schomaecker R. Critical literature review of the kinetics for the oxidative dehydrogenation of propane over well-defined supported vanadium oxide catalysts. *ACS Catal*. 2014;4:3357-3380.

38. Nawaz Z. Light alkane dehydrogenation to light olefin technologies: A comprehensive review. *Rev Chem Eng*. 2015;31:413-436.

39. Bhasin MM, McCain JH, Vora B V., Imai T, Pujadó PR. Dehydrogenation and oxydehydrogenation of paraffins to olefins. *Appl Catal A Gen*. 2001;221:397-419.

40. Wang G, Johannessen E, Kleijn CR, de Leeuw SW, Coppens M-O. Optimizing transport in nanostructured catalysts: A computational study. *Chem Eng Sci*. 2007;62:5110-5116.

41. Coppens MO, Ye G. Nature-inspired optimization of transport in porous media. In: Bunde A, Caro J, Kärger J, Gero V, eds. *Diffusive Spreading in Nature, Technology and Society*. Cham: Springer; 2018:203-232.

42. Munnik P, Jongh PE De, Jong KP De. Recent developments in the synthesis of supported catalysts. *Chem Rev*. 2015;115:6687-6718.

43. Ye G, Sun Y, Zhou X, Zhu K, Zhou J, Coppens M-O. Method for generating pore networks in porous particles of arbitrary shape, and its application to catalytic hydrogenation of benzene. *Chem Eng J*. 2017;329:56-65.

44. Ye G, Duan X, Zhu K, Zhou X, Coppens M-O, Yuan W. Optimizing spatial pore-size and porosity distributions of adsorbents for enhanced adsorption and desorption performance. *Chem Eng Sci*. 2015;132:108-117.

45. Li Q, Sui Z, Zhou X, Chen D. Kinetics of propane dehydrogenation over Pt–Sn/Al_2O_3 catalyst. *Appl Catal A Gen*. 2011;398:18-26.

46. Biswas J, Do DD. A unified theory of coking deactivation in a catalyst pellet. *Chem Eng J*. 1987;36:175-191.

47. Welty JR, Wicks CE, Wilson RE, Rorrer GL. *Fundamentals of Momentum, Heat and Mass Transfer*. 5th ed. Hoboken: John Wiley and Sons; 2008.

48. Poling BE, Prasunitz JM, O'Connell JP. *The Properties of Gases and Liquids*. 5th ed. Boston: McGraw-Hill; 2001.

49. Ruthven DM. *Principles of Adsorption and Adsorption Processes*. New York: Wiley; 1984.

50. Al-futaisi A, Patzek TW. Extension of Hoshen–Kopelman algorithm to non-lattice environments. *Physica A*. 2003;321:665-678.

51. Zangeneh FT, Sahebdelfar S, Bahmani M. Propane dehydrogenation over a commercial Pt-Sn/Al_2O_3 catalyst for isobutane dehydrogenation: Optimization of reaction conditions. *Chinese J Chem Eng*. 2013;21:730-735.

52. Chua LM, Vazhnova T, Mays TJ, Lukyanov DB, Rigby SP. Deactivation of PtH-MFI bifunctional catalysts by coke formation during benzene alkylation with ethane. *J Catal*. 2010;271:401-412.

53. Rao SM, Coppens M-O. Mitigating deactivation effects through rational design of hierarchically structured catalysts: Application to hydrodemetalation. *Ind Eng Chem Res*. 2010;49:11087-11097.

54. Johannessen E, Wang G, Coppens M-O. Optimal distributor networks in porous catalyst pellets. I. molecular diffusion. *Ind Eng Chem Res*. 2007;46:4245-4256.

Table 1. Parameters for a typical simulation.

Number of nodes	2139
Time step (Δt)	250 s
Maximum time for reaction (t_m)	10000 s
Maximum loading of coke (C_{cm})	5×10^{-3} g/m^2
Temperature (T)	838 K
Total pressure (P_t)	1 bar
Bulk pressure of propane ($P_{C_3H_8,b}$)	0.8 bar
Bulk pressure of propene ($P_{C_3H_6,b}$)	0.1 bar
Bulk pressure of hydrogen ($P_{H_2,b}$)	0.1 bar
Total porosity (ε)	0.45
Pore connectivity (Z)	6
Volume-averaged pore radius (r_a)	5×10^{-9} m
Standard deviation of the natural logarithm of the pore radius (σ)	0.5
Internal specific surface area of the catalyst (S_{cat})	93.6 m^2/g
Radius of the catalyst particle (R)	0.002 m
Coke density (ρ_c)	1200 kg/m^3 [a]

[a]Data taken from Chua et al.[52]

List of Figure Captions

Figure 1 An illustration of the three-dimensional pore network within a spherical domain. In this illustration, the pore connectivity is 6, and the number of nodes is 2139.

Figure 2 (a) An illustration of UD1, UD2, and UD3 spatial distributions of pores size for a unimodal catalyst particle; (b) an illustration of BD1 and BD2 spatial distributions of broad pores for a bimodal catalyst particle – here, the blue and grey bonds represent broad and narrow pores.

Figure 3 The change in apparent reaction rate of propene formation over time, and an illustration of the definition of the objective function, given by Eq. (14). The simulation parameters are given in Table 1.

Figure 4 (a) The distributions of coke-plugged pores and (b) concentration profiles of propane in the pore network at different reaction times. A quarter segment of the spherical pore network is cut off to see the details inside the pore network, and the cut surfaces are also displayed. The simulation parameters are given in Table 1.

Figure 5 The effect of porosity (ε) on the time-averaged propene formation rate (R_{obj}) in the catalyst particles under the two assumptions: (a) constant intrinsic activity per unit catalyst weight, (b) constant intrinsic activity per unit internal surface area. Other simulation parameters are given in Table 1.

Figure 6 The effect of pore connectivity (Z) on time-averaged propene formation rate (R_{obj}) of the catalyst particles under the two assumptions: (a) constant intrinsic activity per unit catalyst

weight, (b) constant intrinsic activity per unit internal surface area. Other simulation parameters are given in Table 1.

Figure 7 The effect of volume-averaged pore radius (r_a) on the time-averaged propene formation rate (R_{obj}) in the catalyst particles under the two assumptions: (a) constant intrinsic activity per unit catalyst weight, (b) constant intrinsic activity per unit internal surface area. Other simulation parameters are given in Table 1.

Figure 8 The effect of standard deviation of the natural logarithm of the pore radius (σ) on the time-averaged propene formation rate (R_{obj}) of the catalyst particles under the two assumptions: (a) constant intrinsic activity per unit catalyst weight, (b) constant intrinsic activity per unit internal surface area. Other simulation parameters are given in Table 1.

Figure 9 The effect of total porosity (ε) on the time-averaged propene formation rate (R_{obj}) of the catalyst particles under the two assumptions: (a) constant intrinsic activity per unit catalyst weight, (b) constant intrinsic activity per unit internal surface area. The radius of broad pores is 25 nm, while the radii of narrow pores follow a log-normal distribution (see Eq. (1)). The porosity corresponding to narrow pores is 0.45, and other simulation parameters are displayed in Table 1.

Figure 10 The effect of the broad pore radius (r_B) on the time-averaged propene formation rate (R_{obj}) of the catalyst particles under the two assumptions: (a) constant intrinsic activity per unit catalyst weight, (b) constant intrinsic activity per unit internal surface area. The radii of narrow pores follow a log-normal distribution (see Eq. (1)). The total porosity is 0.70, the porosity

associated to broad pores is 0.45, the porosity corresponding to narrow pores is also 0.45, and other simulation parameters are displayed in Table 1.

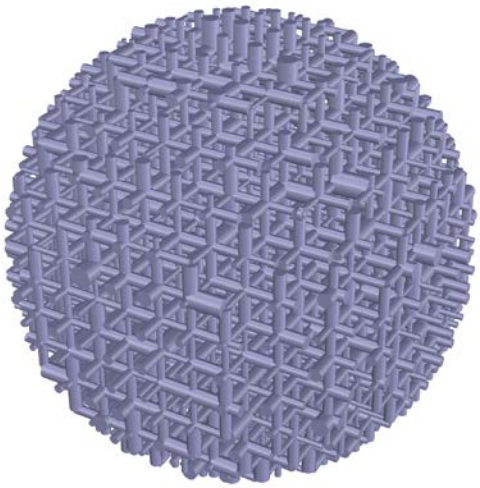

Figure 1 An illustration of the three-dimensional pore network within a spherical domain. In this illustration, the pore connectivity is 6, and the number of nodes is 2139.

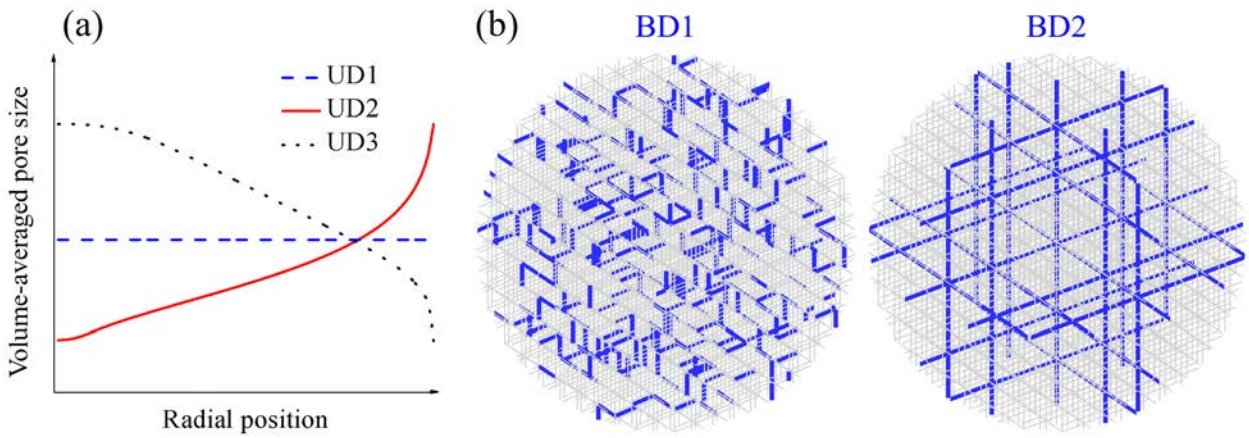

Figure 2 (a) An illustration of UD1, UD2, and UD3 spatial distributions of pores size for a unimodal catalyst particle; (b) an illustration of BD1 and BD2 spatial distributions of broad pores for a bimodal catalyst particle – here, the blue and grey bonds represent broad and narrow pores.

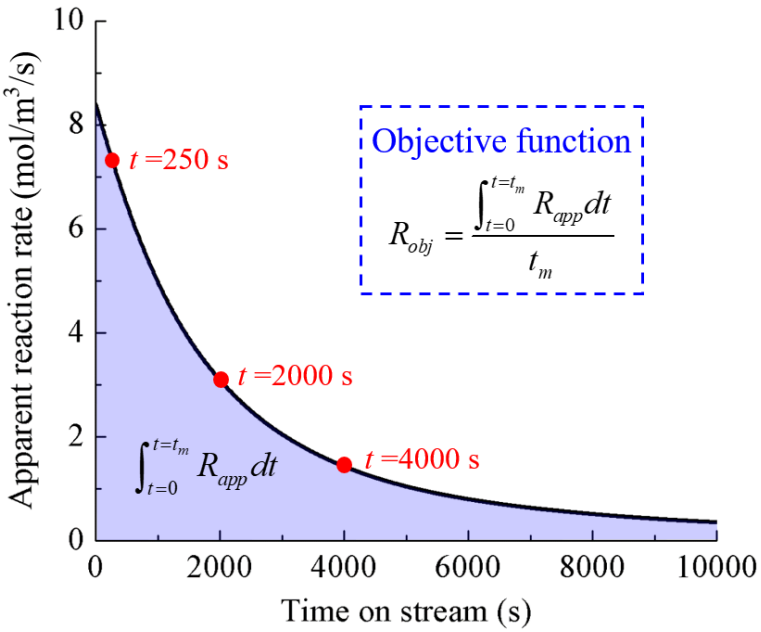

Figure 3 The change in apparent reaction rate of propene formation over time, and an illustration of the definition of the objective function, given by Eq. (14). The simulation parameters are given in Table 1.

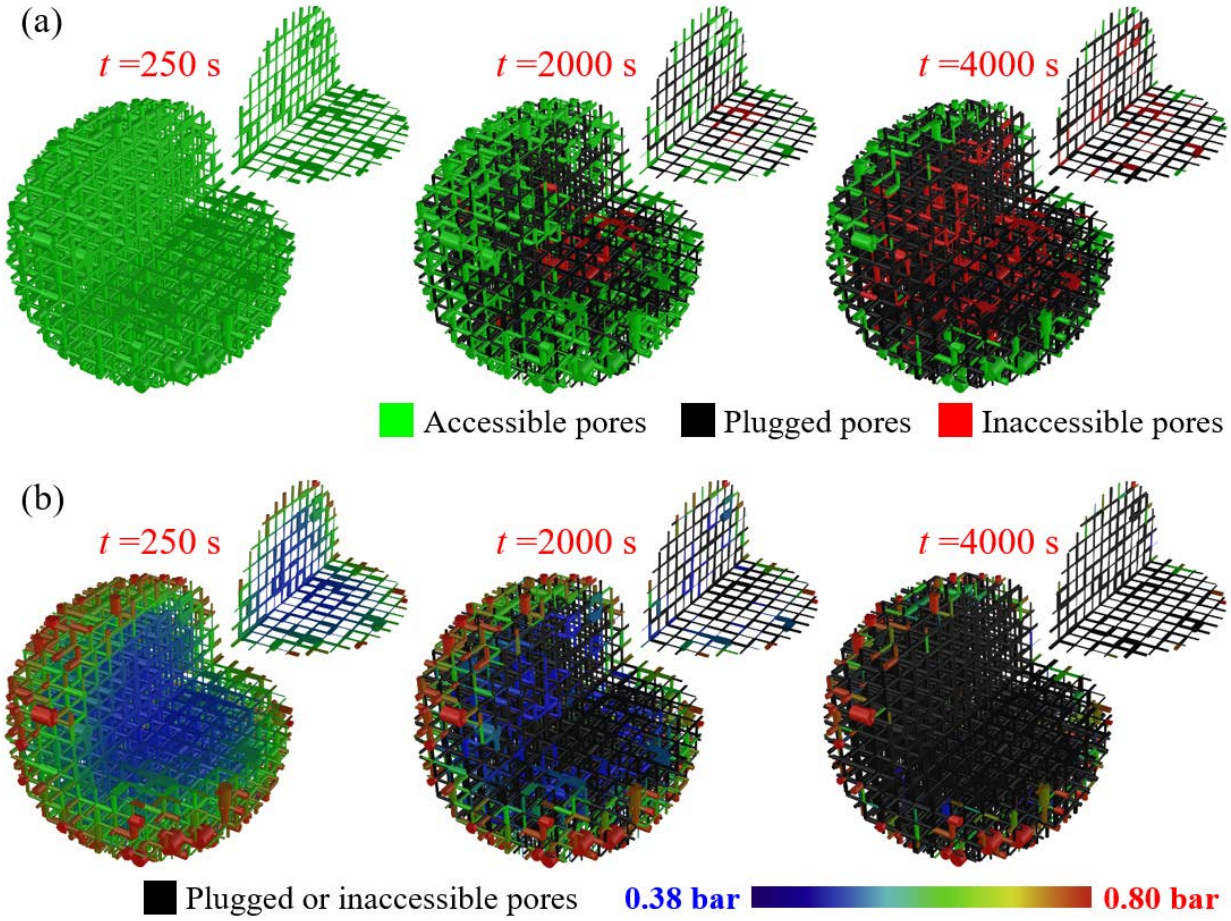

Figure 4 (a) The distributions of coke-plugged pores and (b) concentration profiles of propane in the pore network at different reaction times. A quarter segment of the spherical pore network is cut off to see the details inside the pore network, and the cut surfaces are also displayed. The simulation parameters are given in Table 1.

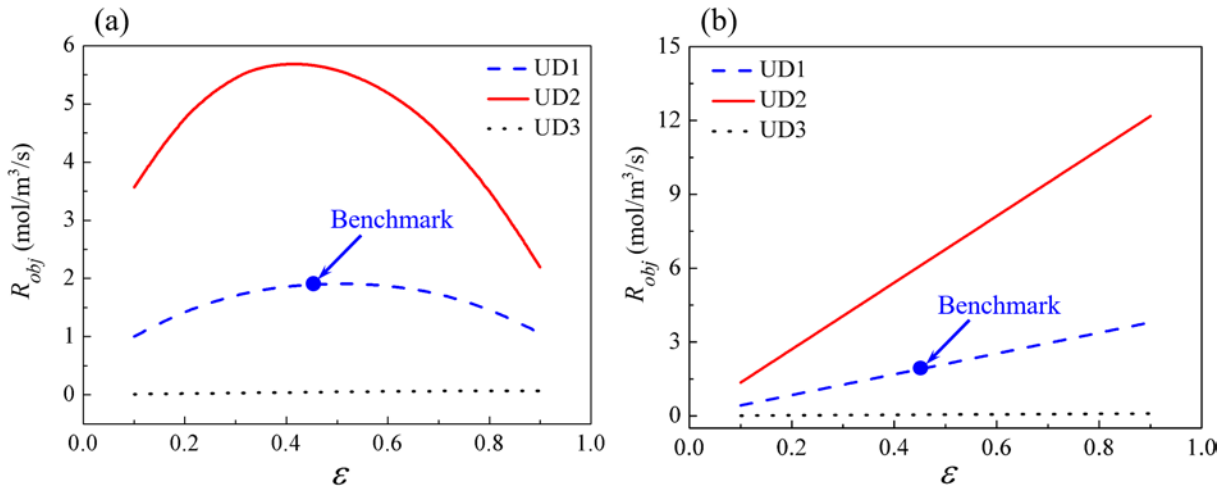

Figure 5 The effect of porosity (ε) on the time-averaged propene formation rate (R_{obj}) in the catalyst particles under the two assumptions: (a) constant intrinsic activity per unit catalyst weight, (b) constant intrinsic activity per unit internal surface area. Other simulation parameters are given in Table 1.

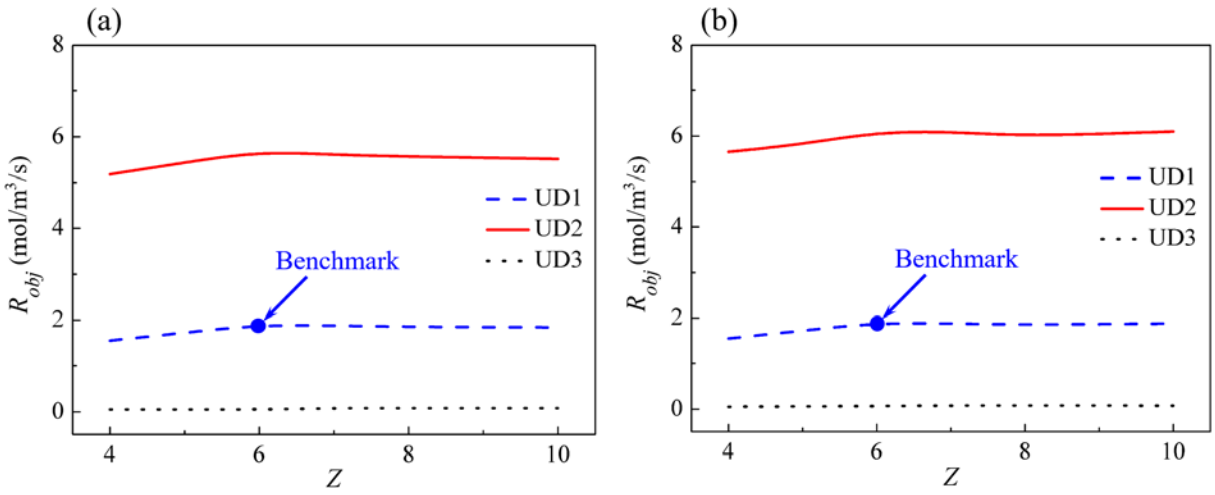

Figure 6 The effect of pore connectivity (Z) on time-averaged propene formation rate (R_{obj}) of the catalyst particles under the two assumptions: (a) constant intrinsic activity per unit catalyst weight, (b) constant intrinsic activity per unit internal surface area. Other simulation parameters are given in Table 1.

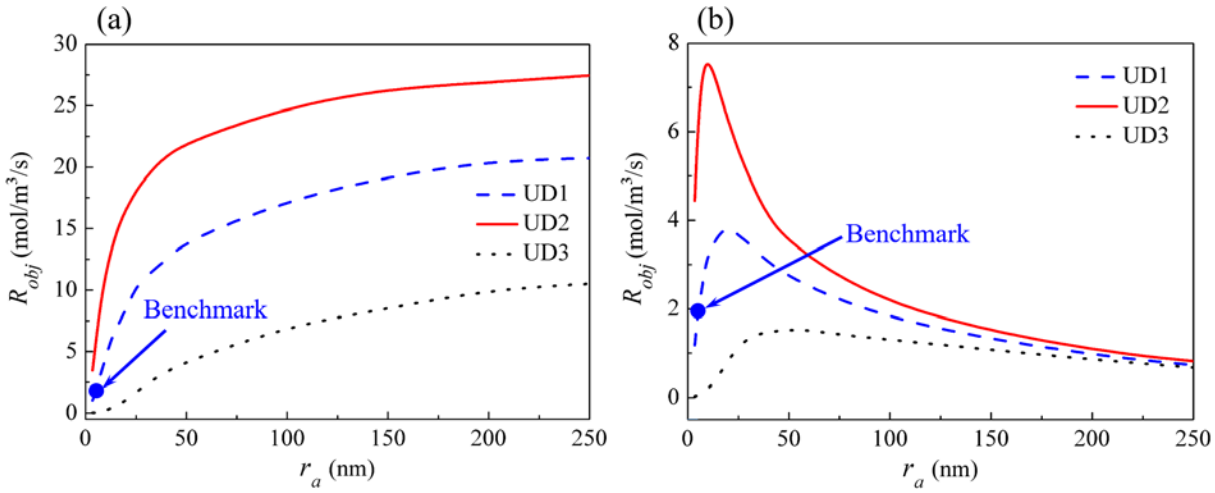

Figure 7 The effect of volume-averaged pore radius (r_a) on the time-averaged propene formation rate (R_{obj}) in the catalyst particles under the two assumptions: (a) constant intrinsic activity per unit catalyst weight, (b) constant intrinsic activity per unit internal surface area. Other simulation parameters are given in Table 1.

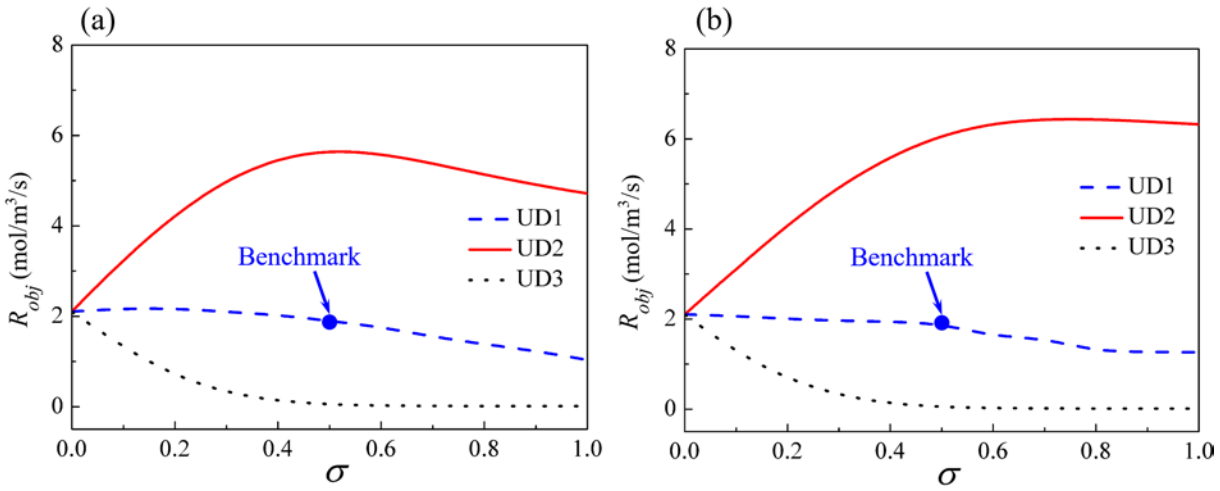

Figure 8 The effect of standard deviation of the natural logarithm of the pore radius (σ) on the time-averaged propene formation rate (R_{obj}) of the catalyst particles under the two assumptions: (a) constant intrinsic activity per unit catalyst weight, (b) constant intrinsic activity per unit internal surface area. Other simulation parameters are given in Table 1.

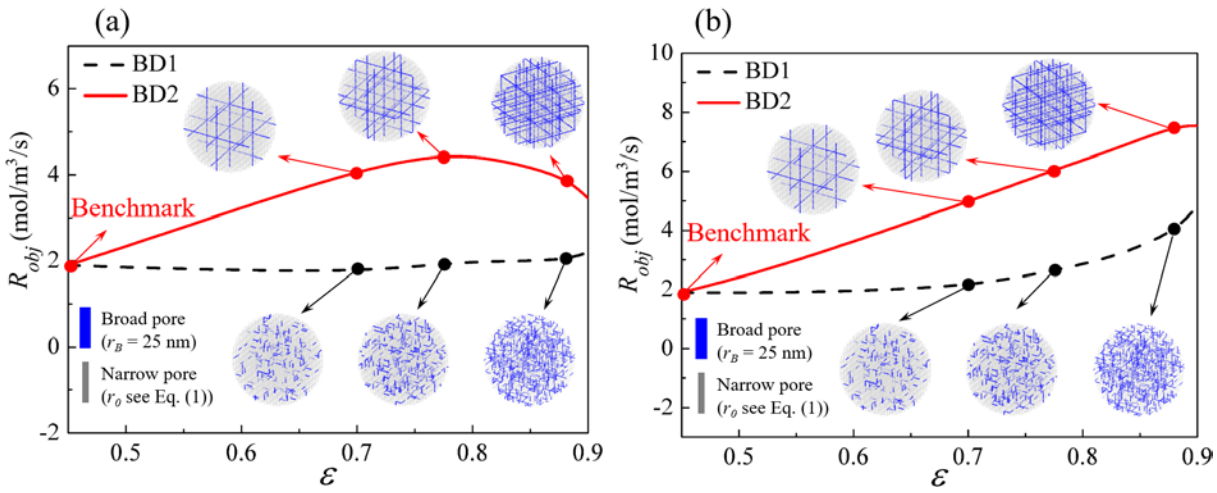

Figure 9 The effect of total porosity (ε) on the time-averaged propene formation rate (R_{obj}) of the catalyst particles under the two assumptions: (a) constant intrinsic activity per unit catalyst weight, (b) constant intrinsic activity per unit internal surface area. The radius of broad pores is 25 nm, while the radii of narrow pores follow a log-normal distribution (see Eq. (1)). The porosity corresponding to narrow pores is 0.45, and other simulation parameters are displayed in Table 1.

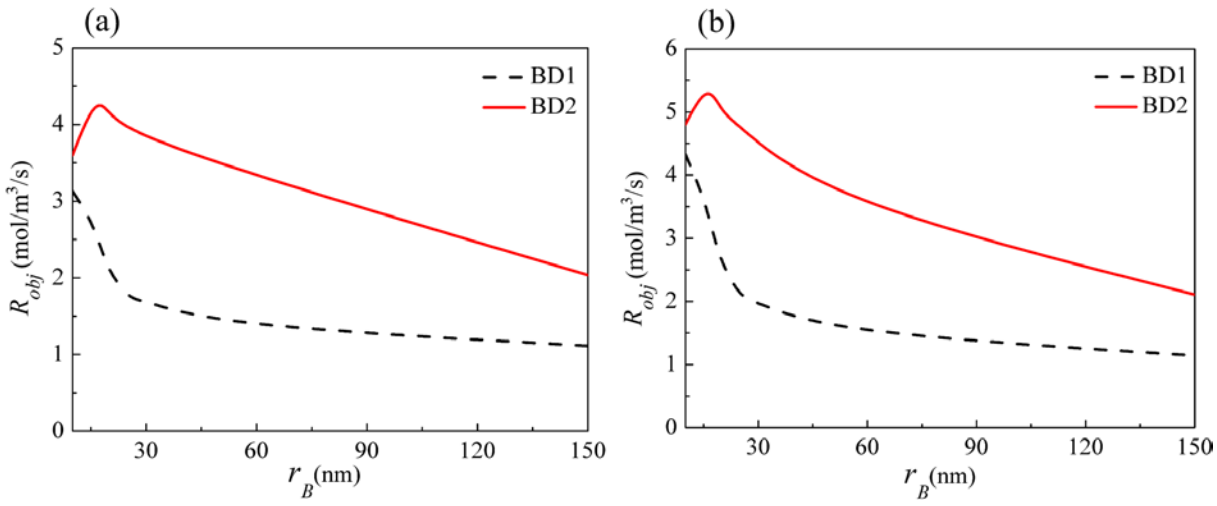

Figure 10 The effect of the broad pore radius (r_B) on the time-averaged propene formation rate (R_{obj}) of the catalyst particles under the two assumptions: (a) constant intrinsic activity per unit catalyst weight, (b) constant intrinsic activity per unit internal surface area. The radii of narrow pores follow a log-normal distribution (see Eq. (1)). The total porosity is 0.70, the porosity associated to broad pores is 0.45, the porosity corresponding to narrow pores is also 0.45, and other simulation parameters are displayed in Table 1.